CONDENSED MATTER PHYSICS

Evidence of ferroelectricity in an antiferromagnetic vanadium trichloride monolayer

Jinghao Deng[1]†, Deping Guo[2,3,4]†, Yao Wen[1]†, Shuangzan Lu[1,5]†, Hui Zhang[1], Zhengbo Cheng[1], Zemin Pan[1], Tao Jian[1], Dongyu Li[1], Hao Wang[1], Yusong Bai[1], Zhilin Li[6], Wei Ji[3,4]*, Jun He[1,7]*, Chendong Zhang[1]*

A reduced dimensionality of multiferroic materials is highly desired for device miniaturization, but the coexistence of ferroelectricity and magnetism at the two-dimensional limit is yet to be conclusively demonstrated. Here, we used a NbSe$_2$ substrate to break both the C_3 rotational and inversion symmetries in monolayer VCl$_3$ and, thus, introduced exceptional in-plane ferroelectricity into a two-dimensional magnet. Scanning tunneling spectroscopy directly visualized ferroelectric domains and manipulated their domain boundaries in monolayer VCl$_3$, where coexisting antiferromagnetic order with canted magnetic moments was verified by vibrating sample magnetometer measurements. Our density functional theory calculations highlight the crucial role that highly directional interfacial Cl-Se interactions play in breaking the symmetries and, thus, in introducing in-plane ferroelectricity, which was further verified by examining an ML-VCl$_3$/graphene sample. Our work demonstrates an approach to manipulate the ferroelectric states in monolayered magnets through van der Waals interfacial interactions.

INTRODUCTION

Spontaneous polarizations in solid-state materials, including spin and electric polarizations, are crucial characteristics for functional device applications. This scenario has been extended to studies of two-dimensional (2D) van der Waals (vdW) materials (1, 2). In the past years, substantial efforts have been made to validate that either a magnetic (3, 4) or ferroelectric (FE) order (5, 6) can be preserved in the 2D limit. These findings immediately stimulated the interest in searching for vdW monolayers (MLs) that can simultaneously incorporate two (or more) ferroic order parameters, with the goal of achieving multiferroicity (MF) at an ML level. This advancement offers prospects for enhanced tunability and flexible integration of polarization configurations with multiple degrees of freedom into complex heterostructures, holding the potential to substantially advance device applications (2). Although quite a few candidates were theoretically predicted to host either type I (7, 8) or type II (9) MF, likely experimental evidence of a multiferroic vdW ML was only revealed for the NiI$_2$ ML based on all-optical methods (10). Recent scanning tunneling microscopy (STM) studies suggest the persistence of spin-spiral order in the ML NiI$_2$ (11), but there remain points of discussion regarding the interpretation of spectroscopic observation related to electric polarization (12). It is still an ongoing project for the dependable and precise determination of its ferroelectricity (13–16). In addition to vdW MLs, the coexistence of ferroelectricity and ferromagnetism was reported for a non-vdW crystal (Cr$_2$S$_3$) with a single-unit-cell thickness (17) during the preparation of this work.

A promising route toward realizing ML MF lies in introducing electric polarizations into known 2D magnets by artificially engineering spatial symmetries. For instance, Huang *et al.* (18) theoretically proposed that Li intercalation or proper charge doping in ML CrBr$_3$ can lead to FE order coexisting with ferromagnetism. Unlike closed-shell Cr^{3+} ions, open-shell V^{3+} ions enable ML vanadium trihalides (VX$_3$) to exhibit mutable orbital ordering, which, in principle, makes them a more feasible material family for tailoring lattice symmetries (19) and, thus, inducing electric polarizations (20). On the experimental side, bulk forms of VX$_3$ are known to be magnetic with either ferromagnetic (FM; VI$_3$) (21–23) or antiferromagnetic (AFM; VCl$_3$ and VBr$_3$) (24–26) configurations. Peculiar orbital orderings (27) and the interplay of magnetic and structural degrees of freedom (28) have also been found in their bulk crystals. At the ML limit, however, experimental exploration is rare, with sporadic studies reported for VX$_3$ MLs (28). Therefore, whether magnetism and electric polarization can be simultaneously retained in ML-VX$_3$ remains unclear.

Here, we epitaxially grow a VCl$_3$ ML on a NbSe$_2$ substrate, in which we report experimental identification of the coexistence of ferroelectricity and antiferromagnetism. Convincing atomic-scale evidence for in-plane (IP) ferroelectricity in the VCl$_3$ ML is obtained through STM/scanning tunneling spectroscopy (STS). This includes key indicators such as severe distortion of the atomic lattice, electric-polarization–induced energy band bending, and tip-induced flipping of the polarization, which collectively verify the presence of ferroelectricity. Moreover, vibrating sample magnetometry (VSM) and density functional theory (DFT) calculations provide consistent evidence that the FE VCl$_3$ ML hosts a bistriped (BS) AFM order ($T_N = 16$ K) with an xz easy plane for magnetization. Our DFT calculations further corroborate that directional interfacial interactions (29, 30), specifically Se-Cl covalent-like quasi-bonds, lead to the spontaneous breaking of the both IP C_3 rotational and out-of-plane (OOP) inversion symmetries. The broken symmetry induced structural distortion results in an appreciable IP total electric polarization

[1]School of Physics and Technology, and Key Laboratory of Artificial Micro- and Nano-structures of Ministry of Education, Wuhan University, Wuhan 430072, China. [2]College of Physics and Electronic Engineering, Center for Computational Sciences, Sichuan Normal University, Chengdu 610101, China. [3]Beijing Key Laboratory of Optoelectronic Functional Materials and Micro-Nano Devices, School of Physics, Renmin University of China, Beijing 100872, China. [4]Key Laboratory of Quantum State Construction and Manipulation (Ministry of Education), Renmin University of China, Beijing 100872, China. [5]Hubei Jiufengshan Laboratory, Wuhan 430074, China. [6]Beijing National Laboratory for Condensed Matter Physics, Institute of Physics, Chinese Academy of Sciences, Beijing 100190, China. [7]Wuhan Institute of Quantum Technology, Wuhan 430206, China.
*Corresponding author. Email: wji@ruc.edu.cn (W.J.); He-jun@whu.edu.cn (J.H.); cdzhang@whu.edu.cn (C.D.Z)
†These authors contributed equally to this work.

and aids in the selective stabilization of magnetic order. To verify our theory, a control experiment is performed on VCl$_3$/graphene where IP ferroelectricity is absent. This work experimentally demonstrates a long-sought integration of ferroelectricity into a magnetic ML through engineering of vdW interfaces.

RESULTS

We started our exploration with molecular beam epitaxy (MBE) growth of VCl$_3$ MLs on freshly cleaved NbSe$_2$ substrates (see Materials and Methods for details). Figure 1A shows a typical STM topography image of an as-grown ML-VCl$_3$ film exhibiting a thickness of ~5.6 Å (fig. S1). A typical tunneling conductance spectrum indicates a 2.08-eV bandgap for the ML, supporting the semiconducting electronic structures calculated in the band structure calculations (20, 31) with the electronic correlation and orbital ordering considered (for detailed tunneling spectra, see figs. S2 and S3). In the prototypical crystalline structure of VCl$_3$, V atoms are arranged in a honeycomb lattice, and each V atom is embedded in an octahedron composed of six Cl

atoms. Therefore, an STM topography showing triangular protrusions is expected for VCl$_3$, akin to those of epitaxial CrBr$_3$ (32) and CrI$_3$ (33). Each of these triangles reflects three top-layer Cl atoms surrounding a threefold rotational symmetry center of the V atom. However, our STM imaging of the VCl$_3$ ML shows distinctively different features. Under a relatively large bias, e.g., 1.5 V, the observed protrusions appear as elongated ovals (Fig. 1B). These oval protrusions form a triangular lattice with a periodicity of 5.96 Å, and the primitive vector **a** is aligned along the armchair direction of NbSe$_2$ (see fig. S4). To simplify the latter discussion, we define orthometric x-y coordinates (as labeled in Fig. 1B) such that y is parallel to vector **a** and x is defined along the armchair (zigzag) direction of the triangular lattice of oval protrusions (NbSe$_2$). An atomically resolved image shown in Fig. 1C, obtained at a smaller bias of −0.35 V, reveals that one oval protrusion is composed of three top-layer Cl atoms, labeled Cl-1, Cl-2, and Cl-3. Notably, the Cl-2 atom is ~0.05 Å higher than the other two Cl atoms in the z direction, as illustrated in a close-up 3D perspective plot (Fig. 1D, top). More intriguingly, Fig. 1C indicates pronounced IP atomic distortion, where the arrangement of Cl-1 to Cl-3 forms a
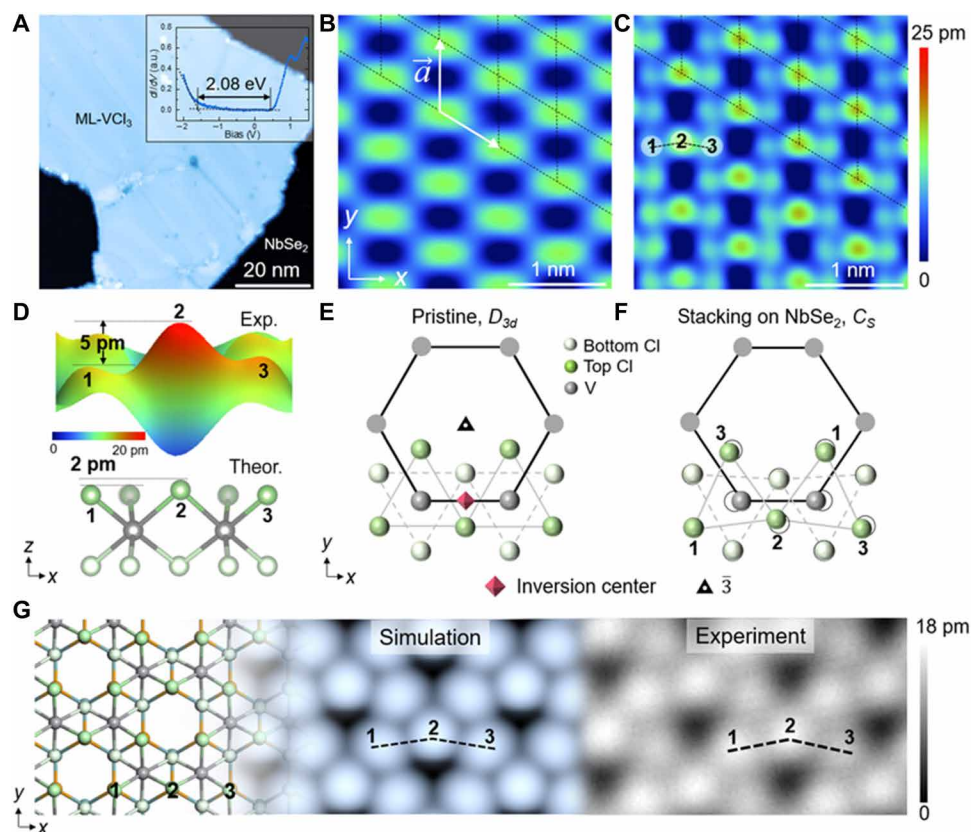

Fig. 1. Morphology and atomic structure of ML-VCl$_3$ on a NbSe$_2$ substrate. (**A**) Large-scale image of an ML-VCl$_3$ flake. Inset: Typical dI/dV spectrum taken on VCl$_3$ (the feedback loop opened at V_b = 1.8 V and I_t = 300 pA with lock-in modulation V_{rms} = 6 mV). The feedback loop opened at V_b = 1.8 V and I_t = 300 pA with lock-in modulation V_{rms} = 6 mV. a.u., arbitrary units. (**B**) A zoomed-in image of VCl$_3$ and (**C**) the corresponding atomically resolved image. The dashed black lines indicate the triangular lattice. x-y coordinates defined with x along the armchair direction; white arrows represent the lattice constant a. Three inequivalent Cl atoms are marked by numbers 1, 2, and 3. A black line connects the three Cl atoms in a boomerang-like shape. (**D**) Three-dimensional image zoomed in on a boomerang (top) and a side view of the calculated atomic model (lower panel). The V, top-layer Cl, and bottom-layer Cl atoms are shown in gray, dark green, and bright green, respectively. (**E** and **F**) Schematics of pristine VCl$_3$ and NbSe$_2$-supported VCl$_3$, respectively. The NbSe$_2$ lattice is not displayed for simplicity. The red rhombus and black triangle represent the inversion symmetry and threefold rotational symmetry centers, respectively. (**G**) Comparison of the DFT structure (left), the simulated STM image (middle, simulated under −2.0 V bias), and the experimental STM image. The Nb and Se atoms are shown in blue and orange, respectively. Scanning parameters V_b and I_t are (A) 1.5 V and 20 pA, (B) 1.5 V and 50 pA, (C) −0.35 V and 50 pA, and (G) −2 V and 50 pA.

boomerang-like structure. This configuration is distinctly different from trimerized morphology characterized by an equilateral triangle in Cr-based trihalides (*32–34*). In this boomerang arrangement, we define the direction of the protruding Cl-2 atom as the +y direction.

Our DFT calculations reproduce this unusual morphology observed in STM. Figure 1E shows a schematic model of a freestanding pristine VCl$_3$ ML, while Fig. 1F illustrates the fully relaxed atomic structure of the most energetically favored stacking configuration of the VCl$_3$ ML grown on NbSe$_2$ (see the detailed discussion in fig. S6). Upon stacking on NbSe$_2$, the OOP inversion symmetry is lifted. In addition, the IP C_3 rotational symmetry is also broken owing to interfacial interactions (as elucidated later) that appreciably distort the V-Cl$_6$ octahedra. For clearer visualization, the lattice distortions are slightly exaggerated in Fig. 1D. Such distortion shifts the top-layer Cl atoms off their original positions, allowing us to identify the experimentally defined Cl-1 to Cl-3 atoms in the theoretical model (Fig. 1, D and F). The middle Cl-2 atom sits higher than the Cl-1 and Cl-3 atoms by 0.02 Å in the calculations (0.05 Å in the experiments), and there is a lateral shift of the Cl-2 atom in the +y direction, forming an IP boomerang-like arrangement. The validity of the theoretical model is further verified by a one-to-one comparison of simulated and experimental constant-current STM images (Fig. 1), while the detailed mechanism for the formation of this distorted structure on NbSe$_2$ will be discussed later. Note that Fig. 1C was obtained following a formerly adopted methodology for scanning ultrathin insulating/semiconducting layers on metallic substrate, specifically by scanning within the band gap (*35*). This approach helps minimize the impact of spatially varying electronic states on the measurement of morphological heights. Meanwhile, the parameters for comparison in Fig. 1G, which focus on IP morphology, are set at energy levels outside the bandgap to enable theoretical simulations.

Figure 2A shows a magnified image of the VCl$_3$ flake shown in Fig. 1A, which exhibits a series of parallel boundaries. Two types of domain walls (DWs) were distinguished under a scanning bias of V_b = 1.5 V, showing alternating bright (DW-S) and dark (DW-I) DWs. Figure 2 (B and C) shows atomically resolved STM images of DW-S and DW-I, respectively. At DW-S, two adjacent Cl boomerangs share a common Cl atom (Fig. 2D), while, at DW-I, an isolated Cl atom separates two adjacent Cl boomerangs. The topology of the atomic lattice is continuous across both DW-S and DW-I (see fig. S7 for details), excluding the possibility of dislocation defects. In addition, the lattice distortions, which are characterized by the +y directions of Cl boomerangs, as labeled in Fig. 2 (B and C), are always mirror symmetric in the adjacent domains, and DW-S and DW-I correspond to the tail-to-tail and head-to-head configurations of the +y coordinates. For simplicity, we used these parallelly aligned DWs in the following discussion, although they are not necessarily parallel, as the lattice distortion is sixfold degenerate in ML-VCl$_3$ (see figs. S8 and S9 for details).

The alternating bright and dark topographic contrasts of DWs (Fig. 2A) suggest spatial variations in the local density of states across the DWs. Figure 2E shows a color-coded rendering of the band mapping taken along a pathway across three DWs (white dashed line in Fig. 2A). We used the conduction band, sitting ~1.5 eV above the Fermi level, for illustration, which is more evident than the valence band, to show the spatial variation in electronic states (fig. S2). Clear band bending was observed within each domain. The energy level of the energy band, i.e., the ~1.5 eV conduction band, near DW-S is always higher than that near DW-I. An energy shift of 57 meV was determined by comparing two selected spectra extracted near DW-S and DW-I (Fig. 2F). Noticed that the onset of band edge in Fig. 2F shows slight difference to the tunneling spectrum in Fig. 1A due to the larger tip-sample distance. The reproductivity of the band bending has been verified by multiple different tips across different samples. Detailed discussion on the influence of different spectroscopic parameters and in the near nonparallel region can be found in figs. S10 and S11.

This band bending suggests that DW-S and DW-I are most likely negatively and positively charged. Figure 2G shows a schematic summarizing the charge accumulation and band bending at the DWs. Noticed that band bending behaviors between DWs do not show apparent dielectric screening effects (*5*), which can be ascribed to the relatively narrow domains here. In fig. S12, we show that substantially different band bending behaviors are also observable between opposite edges of the ML-VCl$_3$ flakes (*36*). The estimated screening length in fig. S12 is around 4 to 5 nm, which further supports our non-screening scenario because the spacing between DWs is only ranging from 6 to 10 nm. These lattice deformation–linked changes in the charge polarities at DWs and/or edges were widely adopted in previous STM studies to recognize IP electric polarizations in 2D layers (*5, 36, 37*).

Besides the band bending induced by net electric polarization, another key criteria in STM studies to justify the existence of FE order is the external field–controlled manipulation of its direction (*5, 38*). This criterion holds true even for IP FE case, such as in studies of SnSe (*39*), where local electric field between the conductive tip and a sample can include an IP component. In fig. S13, we demonstrate that, under specific tunneling conditions, the IP component of the applied electric field can reversibly switch the direction of lattice distortion in ML-VCl$_3$. This switching induces the controllable movement of DWs and serves as evidence of manipulating local IP electric polarization due to the established correlation between polarization and lattice distortion direction. On the basis of all above discussions and findings, the conclusion that ML-VCl$_3$ exhibits IP ferroelectricity is supported by a comprehensive and rigorous body of experimental evidence. In terms of the polarization vector **P**, our STS measurements can only reveal the component perpendicular to the DWs, namely, **P**$_\perp$, which was experimentally derived to be ~0.04 μC cm^{-2} (see Materials and Methods for details). This polarization strength is comparable to that of known FE vdW layers, such as bilayer WTe$_2$ (~0.19 μC cm^{-2}) (*6*) and twisted bilayer graphene/hBN (~0.1 μC cm^{-2}) (*40*). Meanwhile, the ferroelectricity arising from structural distortions generally exhibits a high transition temperature. Our current experimental evidence suggests that the transition temperature of VCl$_3$ ferroelectricity is at least above liquid nitrogen temperature and is stable under magnetic field (fig. S14).

Next, we performed VSM measurements to investigate the magnetic properties of this FE VCl$_3$ ML (details are discussed in Materials and Methods and figs. S14 to S16). The magnetization-temperature (*M-T*) curves are plotted in Fig. 3A for both zero-field cooling (ZFC) and field cooling (FC) procedures, in which the magnetic field (μ$_0$$H$) reached 1 T. Both *M-T* curves coincide well with each other. An AFM order was characterized by a rapid decrease in magnetization (*M*) with a decrease in temperature (*T*) to below the transition temperature T_N. The T_N value was subsequently determined to be T_N = 16 K by extracting the linear onset of the *dM/dT* curve (Fig. 3B), which is close to the AFM transition temperature of 20 K for bulk VCl$_3$ (*24, 26*). The *M-H* measurements (Fig. 3C) further support
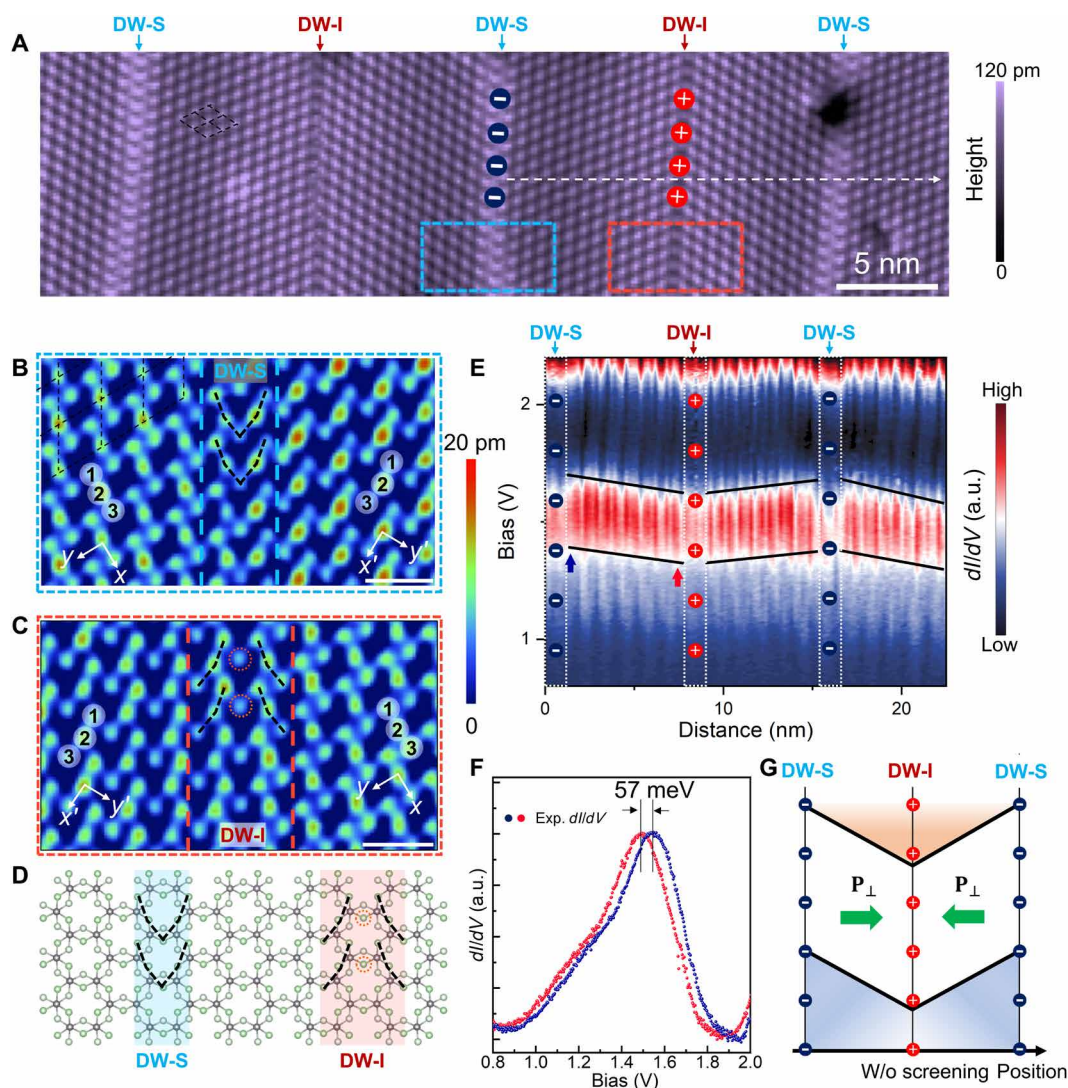
Fig. 2. IP electric polarizations characterized by band bending near DWs. (**A**) Image of parallel DWs in ML-VCl₃ with DW-I and DW-S marked by "+" and "−" signs for polarization charges. (**B** and **C**) Atomically resolved images of DW-S and DW-I, respectively, with dashed grids for unit cells and black boomerang-like lines for the Cl trimers. The x (x')–y (y') coordinates indicate different orientations of atomic displacements in neighboring domains. Blue and red dashed lines were added as guides to the eyes of the locations of DWs. (**D**) Schematic model of DW-S and DW-I. The Cl boomerangs are represented by black dashed zigzag lines in (B) to (D), and isolated Cl atoms in DW-I are marked by red circles in (C) and (D). (**E**) Spatially resolved dI/dV spectra acquired along the white arrow in (A). The feedback loop opened at $V_b = 2.2$ V and $I_t = 200$ pA with lock-in modulation $V_{rms} = 6$ mV. The positions of DWs are marked by + and − markers and white dashed lines. (**F**) Two selected dI/dV spectra, corresponding to positions marked in (E) and plotted in matching colors. (**G**) Schematic model of the IP electric polarization–induced band bending without screening. The green arrows and $\mathbf{P}_\perp$ denote the components of the polarization vector perpendicular to the DWs. Scanning parameters V_b and I_t: (A) 1.5 V and 100 pA and [(B) and (C)] −0.35 V and 50 pA. Scale bars, 1 nm [(B) and (C)].

the discovered AFM order (*41*, *42*), despite the weak FM features observed near the zero-field region (details are shown in figs. S15 and S16). In previous studies (*43*, *44*), similar FM features were ascribed to the graphene substrates used for VSM measurements, which were also observed in our measurements on bare substrates with graphene layers (see detailed discussion in fig. S15). For all our measurements, the magnetization-field curves show similar features for both the IP and OOP magnetic fields, indicating canted magnetic moments in the AFM VCl₃ MLs. Theoretically, we considered four typical magnetic orders for NbSe₂-supported ML-VCl₃, as displayed in Fig. 3D, the total energies of which are plotted in Fig. 3E. The BS AFM order

is at least 2 meV more stable than the other orders. The magnetic moments of the BS AFM configuration preferably orient in the xz easy plane, exhibiting a negligible (0.005 meV/VCl₃) energy difference within the plane (Fig. 3F), while rotating the moments to the y axis increases the total energy by 0.10 meV/VCl₃. The magnetic anisotropy revealed by DFT is well consistent with the VSM results. All these results indicate that BS AFM order with an xz easy plane formed in our ML-VCl₃. Our theoretical calculations also indicate that the preferred magnetic configuration and the electric polarizations are correlated with the atomic structure deformations (see fig. S18 for details).
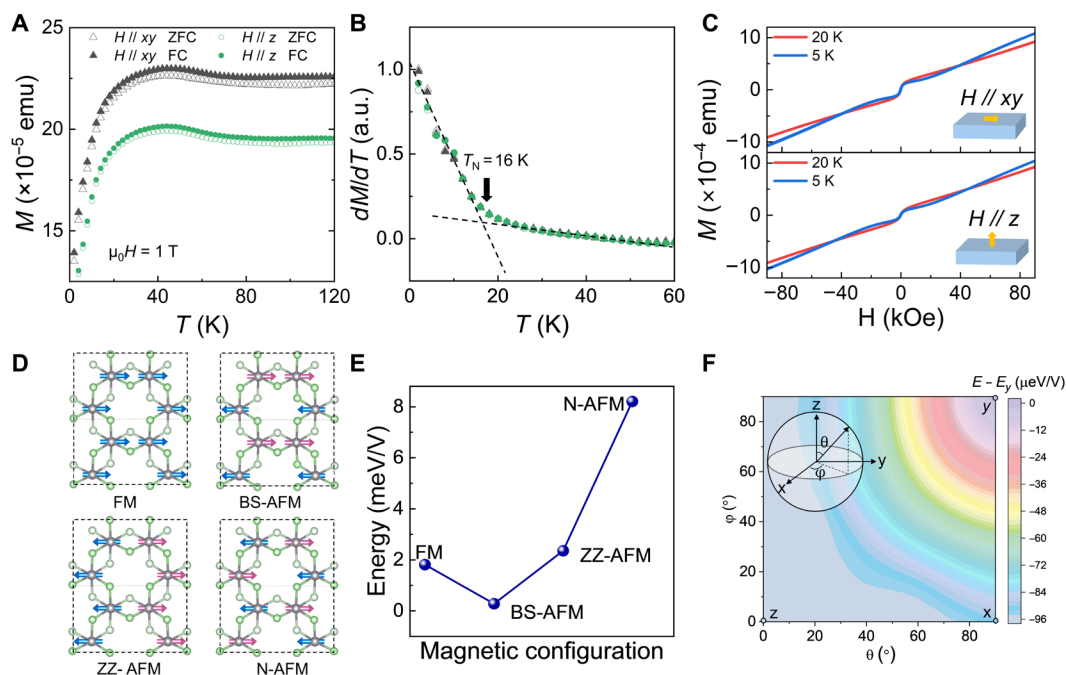
Fig. 3. Experimental and theoretical investigations of the magnetic order in epitaxy ML-VCl$_3$. (**A**) M-T curves taken under IP (black) and OOP (green) magnetic fields ($H = 1$ T). ZFC and FC data are shown as hollow and solid dots, respectively. (**B**) dM/dT data for determining the AFM transition temperature T_N. (**C**) Top (bottom) panels show M-H curves taken under IP (OOP) magnetic fields. The red and blue curves correspond to the magnetization curves acquired at temperatures above and below T_N (i.e., 20 and 5 K, respectively). The details are shown in fig. S12. emu, electromagnetic unit. (**D**) Illustrations of the ferromagnetic (FM), bistriped (BS), zigzag (ZZ), and Néel (N) AFM configurations of ML-VCl$_3$ on NbSe$_2$. The NbSe$_2$ lattice is not displayed for simplicity. The green and gray balls represent Cl and V atoms, respectively. (**E**) Plot of relatively total energies for the four magnetic configurations. (**F**) Magnetic anisotropy energy mapping of ML-VCl$_3$ on NbSe$_2$ with the BS AFM configuration. The coordinate system was defined as shown. The zero energy is defined by the configuration in which the magnetic moments align parallel to the y-direction.

We next discuss the most likely origin(s) of the associated IP ferroelectricity. The preferred BS-AFM configuration results in two types of interfacial Cl atoms, namely, Cl_A and Cl_B1 (Cl_B2), denoted by the green background white letters A and B1 (B2) in the spin-density plot shown in Fig. 4A. Atom Cl_A is sandwiched by two spin-density contours of the same component (yellow isosurface) and lacks spin density in the positive y direction. However, the two-neighboring spin-density contours of atom Cl_B1 (Cl_B2) are in different spin components (one yellow and one blue isosurface).

This unbalanced spin-density distribution indicates the IP C_3 rotational symmetry breaking in the VCl$_3$ overlayer, which induces at least three categories of electron redistribution at the Cl-Se interfaces, as illustrated by the interfacial differential charge density (DCD) at the VCl$_3$-NbSe$_2$ interface (Fig. 4, B and C). An approximate yz mirror plane could be identified from either the spin density (Fig. 4A) or the DCD (Fig. 4B), where interactions involving Cl_B1 and Se_B1 (orange background white letter B1 hereinafter) are nearly mirror symmetric with those involving Cl_B2 and Se_B2, respectively, e.g., Cl_A-Se_B1 is mirror symmetric with Cl_A-Se_B2. This approximate mirror symmetry requires that the atomic displacements of VCl$_3$ along the x direction are nearly mirror symmetric. As a result, the atomic displacements inducing IP electric dipole moments nearly cancel each other under this approximate mirror reflection, as we illustrated quantitatively later.

The mirror plane is parallel to the y direction, meaning that the approximate mirror symmetry does not affect electric dipole moments along the y direction. Along path Cl_A-Se_B1 (blue dashed lines in Fig. 4, B and C), only charge accumulation appears (Fig. 4C). However, directional charge reduction is primarily observed along path Cl_A-Se_A (denoted by the red dashed lines in Fig. 4, B and C), and alternating charge accumulation and reduction are found along path Cl_B1-Se_B1 (violet dashed line in Fig. 4D). These different charge variations at the Cl-Se interface potentially induce anisotropic atomic displacements for the interfacial Cl atoms and, thus, likely IP electric polarization in the y direction.

In Fig. 4E, we plot the color-coded distribution of the atomic displacements in the y direction with respect to the pristine atomic structure of ML-VCl$_3$. The enhanced electron density along path Cl_A-Se_B1 (Fig. 4C) pulls these two atoms away from each other, while the alternating charge accumulation and reduction provide relatively more attractive interactions between Cl_A and Se_A (Cl_B1 and Se_B1). Therefore, the overall result leads to Cl_A undergoing a negative displacement (darkest area in Fig. 4E) and Cl_B1 (Cl_B2) undergoing a slightly positive shift (brighter areas in Fig. 4E) relative to the y axis). As the structures of interfacial and surface Cl atoms are locked by the V-Cl$_6$ octahedron, the surface Cl atoms are shifted upward for A$_u$ (brightest area in Fig. 4E) and moved slightly downward for B1$_u$ and B2$_u$ (darker areas) in the y direction, which were observed in our STM imaging and DFT simulations.

This nonsymmetric displacement field of cations/anions leads to an ionic contribution of $(-0.063, 0.072)$ μC cm^{-2} to the $(\mathbf{x}, \mathbf{y})$ vector of the electric polarization. This ionic polarization is well screened, particularly in the x direction, well screened by electrons within the ML-VCl$_3$, for which the calculated electronic contribution is (0.060,
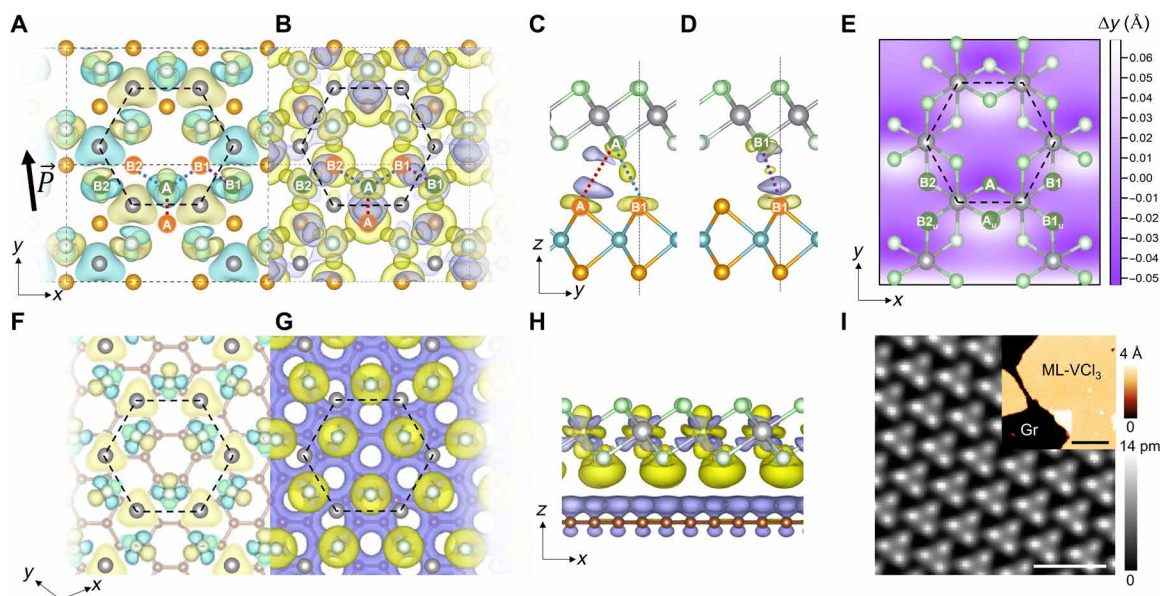
Fig. 4. Anisotropic charge transfer–induced IP ferroelectricity and comparison with the VCl$_3$-graphene interface. (**A**) Top view of the spin density at the VCl$_3$-NbSe$_2$ interface. Only V atoms, top-layer Se atoms, and bottom-layer Cl atoms are shown. The V, Se, and Cl atoms are shown in gray, orange, and light green, respectively. The yellow (blue) isosurface represents spin up (down), and an isosurface value of 1.2×10^{-4} e/bohr^3 was used. The black arrow in (A) indicates the polarization direction $\vec{P}$. (**B**) Top view of the DCD at the VCl$_3$-NbSe$_2$ interface. A yellow (purple) isosurface represents charge accumulation (reduction). The blue dashed lines represent Coulomb repulsion, and the red dashed line represents Coulomb attraction. (**C** and **D**) Side views of DCDs at the VCl$_3$-NbSe$_2$ interface solely along path Cl_A-Se_A (red dashed line), Cl_A-Se_B1 (blue dashed line) (C), or Cl_B1-Se_B1 (violet dashed line) (D). (**E**) Atomic displacements in the y direction in NbSe$_2$-supported VCl$_3$. The displacements were extracted with respect to the pristine atomic structure. Top (bottom)–layer Cl atoms are marked by A$_u$ (A), B1$_u$ (B1), and B2$_u$ (B2). (**F** and **G**) Top view of the spin density and DCD at the VCl$_3$-graphene interface. (**H**) Side view of the DCD at the VCl$_3$-graphene interface. A freestanding bilayer graphene is used in this model with only the top layer displayed. An isosurface value of 3×10^{-4} e/bohr^3 was used. Carbon atoms are shown in brown. (**I**) Atomically resolved STM image of ML-VCl$_3$ grown on an graphene/SiC substrate ($V_b = 0.5$ V and $I_t = 50$ pA; scale bar, 1 nm). The inset shows a large-area image, where Gr represents the graphene substrate ($V_b = 1.5$ V and $I_t = 20$ pA; scale bar, 20 nm).

-0.055) μC cm^{-2}. However, the electronic screening is insufficient to fully compensate for the electric polarization along the y direction, leaving a net polarization of 0.017 μC cm^{-2} [(-0.002, 0.017) μC cm^{-2}]. Additional screening from interfacial and substrate electrons maintains the electric polarization along the x direction, keeping its variation within 0.001 μC cm^{-2}. In contrast, screening from the substrate further suppresses the polarization along the y direction, reducing it to 0.014 μC cm^{-2} [(-0.003, 0.014) μC cm^{-2}], which is consistent with the polarization values and the polarization direction observed in our experiments.

In short, the IP polarization originates from the incomplete electronic screening of the asymmetric atomic displacements that induce polarization along the y direction in the VCl$_3$ overlayer. Such incomplete electronic screening is a well-known feature in 2D materials due to their reduced dimensionality (*45*). These asymmetric atomic displacements are primarily driven by the directional Cl-Se interfacial interactions, often referred to as covalent-like quasi-bonding (*30*, *46*, *47*). This quasi-bonding involves the overlap and hybridization of frontier orbitals between adjacent vdW layers but differs substantially from true covalent bonds, as the electron population in the hybridized bonding and antibonding states remains balanced. Thus, despite the enhanced interfacial electronic interactions, the VCl$_3$ ML preserves its 2D character on the NbSe$_2$ substrate, as observed in previous studies on other 2D vdW heterojunctions (*48*, *49*). Furthermore, the open-shell configuration of V^{3+}, with two d-electrons occupying three t_{2g} orbitals, is another essential factor,

which contributes to the fragility of the IP C_{3v} symmetry. Thus, sufficient directional Cl-Se interfacial interactions can break this symmetry, leading to IP structural distortions, favoring a particular orbital ordering and, consequently, a preferred magnetic order (*50*).

It is of importance to emphasize that this interface-engineered ferroelectricity is distinct from sliding ferroelectricity. In the latter, OOP polarization arises from breaking of inversion symmetry due to interlayer atomic mis-registry, while polarization reversal (i.e., DW motion) results from subtle shift in atomic registry due to sliding (*51*). Our case involves lattice distortion-induced electric polarization, which belongs to type I multiferroics like BiFeO$_3$ (BFO) and BiMnO$_3$, where ferroelectricity is not directly derived from magnetism. Most type I multiferroics exhibit weak magnetoelectric couplings, limiting their applications. However, BFO is an exception allowing electric-field control of magnetic domains through its moderate coupling (*52*). ML-VCl$_3$ also has an atomic structure–mediated appreciable correlation between ferroelectricity and magnetism due to its orbital ordering (fig. S18).

To verify the crucial role that the directional interaction plays in the IP electric polarization at the VCl$_3$-NbSe$_2$ vdW interface, we theoretically constructed a VCl$_3$ ML on graphene substrate governed by nondirectional interfacial interactions (*53*). Analogous to Fig. 4 (A to D), the spin density, the top view of the interfacial DCD, and the side view of the interfacial DCD are plotted for the VCl$_3$/graphene heterostructure in Fig. 4 (F to H), respectively. Both top views (Fig. 4, F and G) indicate that the C_3 rotational symmetry is nearly maintained

for VCl_3 on the graphene substrate. While an OOP interface dipole forms at the VCl_3-graphene interface (Fig. 4H), the induced IP charge variation is, unlike in the $NbSe_2$ case, nearly isotropic and directionless (Fig. 4, F and G). Similar isotropic IP interfacial interactions were previously observed at metal-graphene interfaces (53, 54). In the present case, the heterojunction provides an OOP polarization of -1.76 μC cm^{-2} and a nearly zero IP polarization. Noted that such nondirectional interfacial interactions with graphene remain consistent regardless of the specific magnetic configuration in VCl_3 (see details in fig. S19). Controlled experiments were also performed via growth of a VCl_3 ML on a graphene/SiC substrate (Materials and Methods). Figure 4I shows a typical STM image of ML-VCl_3 grown on graphene/SiC, which indicates that the atomic structure, at least for the surface Cl atoms, is not appreciably distorted and exhibits no polarized domains or well-defined DWs, consistent with our calculated results of the VCl_3/graphene heterostructure (refer to fig. S20 for additional experimental data).

DISCUSSIONS

In conclusion, we observed IP electric polarizations in a magnetic VCl_3 ML selectively grown on a $NbSe_2$ substrate. By combing STM, VSM, and first-principles calculations, we explicitly demonstrate the coexistence IP ferroelectricity and canted BS antiferromagnetism. Moreover, we reveal that interfacial Cl-Se interactions in the VCl_3-$NbSe_2$ heterojunction break both the IP C_3 rotational and the OOP inversion symmetries, inducing an IP ferroelectricity. Controlled experiments and calculations for the VCl_3-graphene interface verified this mechanism for introducing ferroelectricity, in which vdW interfacial interactions seem to play an elegant role in tailoring the crystalline symmetry and its related emergent quantum phases. Our findings not only provide a potential ML platform for MF but also refresh the understanding of vdW interface engineering in controlling functional polarizations through multiple degrees of freedom.

MATERIALS AND METHODS
Sample preparations
The sample growth was carried out within an ultra-high-vacuum (UHV)-MBE system with a base pressure of ~2.4×10^{-10} torr. High-quality VCl_3 powder (99.5%) was evaporated by a homebuilt Knudsen cell evaporator. The flux rate was measured to be ~0.15 ml/hour at a growth temperature of 523 K. A fresh $NbSe_2$ surface was acquired by cleaving a bulk $NbSe_2$ crystal in a UHV load-lock chamber at room temperature. During the growth of ML-VCl_3 on $NbSe_2$, the substrate temperature was held at 420 K. Postannealing procedures were performed for 1 hour at 420 K to ensure high-quality crystallization. The growth of ML-VCl_3 on graphene and ML-$NbSe_2$ substrates involved growth parameters identical to those for growth on bulk $NbSe_2$. Graphene layers were prepared on 4H-SiC(0001) wafers by a well-established method of vacuum annealing (55). Single-layer or bilayer graphene could be selectively formed on the SiC(0001) surface by controlling the annealing time (55). Single-layer graphene was used for direct VCl_3 deposition (the samples presented in Fig. 4D and fig. S13), and bilayer graphene was used for preparing ML-$NbSe_2$ (i.e., the substrates used in VSM measurements). ML 1H-$NbSe_2$ was grown on graphene/SiC following a previously reported method (56). High-quality Nb (99.5%) and Se (99.999%) were evaporated by an electron-beam evaporator and a

homebuilt Knudsen cell evaporator, respectively. The flux ratio between Nb and Se was ~1:20, while the substrates were held at 773 K during deposition. To protect the sample from degradation in air, 10-nm Se capping layers were deposited on ML-VCl_3 at room substrate temperature before moving it from the ultrahigh vacuum environment to perform VSM measurements.

STM/STS and VSM measurements
The STM/STS measurements were carried out on a commercial Unisoku-1300 system. All the measurements were taken at the liquid helium temperature (~4.3 K). The PtIr tips used in this work were calibrated by measuring the surface state of a Cu (111) crystal. Tunneling spectroscopies were performed by utilizing a standard lock-in amplifier with a modulation frequency of 932 Hz. The modulation voltages used are specified in the figure captions. STM images were processed using Gwyddion (57). Magnetic susceptibility measurements were performed in the Quantum Design PPMS DynaCool with a VSM option. To enhance the signal strength, we stacked 12 pieces of 2 mm–by–2 mm ML-VCl_3/$NbSe_2$ samples together. ZFC and FC measurements were performed in both IP and OOP directions at 1 T, covering a temperature range from 2 to 390 K with increments of 2 K for each step. Magnetization measurements were carried out by sweeping the magnetic field from -9 to 9 T at various temperatures.

DFT calculations
Calculations were performed using the generalized gradient approximation in the Perdew-Burke-Ernzerhof (PBE) form (58) for the exchange-correlation potential, the projector augmented wave method (59), and a plane-wave basis set as implemented in the Vienna Ab initio Simulation Package (60). Grimme's D3 form vdW correction was considered with the PBE exchange functional (PBE-D3) (61) in all structural relaxations. On-site Coulomb interactions of the V d orbitals were considered using a DFT+U method (62) with $U = 3$ eV, consistent with the values used in the literature (20, 31, 63). The structures were fully relaxed until the residual force per atom was less than 0.005 eV/Å. A plane-wave energy cutoff of 450 eV was adopted for the structural relaxation calculation. A k-mesh of $7 \times 13 \times 1$ ($5 \times 5 \times 1$) was used to sample the first Brillouin zone of VCl_3 on $NbSe_2$ (graphene). All the vacuum layers adopted (>15 Å) were sufficient to appreciably reduce the image interactions. A $\sqrt{3} \times 1$ rectangular lattice (2×2 hexagonal lattice) was adopted for VCl_3 on $NbSe_2$ (graphene). Two-layer $NbSe_2$ (graphene) was used to model the substrate, in which the bottom layer was kept fixed and the top layer was allowed to fully relax. Atomic position projections were obtained by subtracting the corresponding atomic positions of bare VCl_3 with inversion symmetry from the structure of VCl_3 relaxed on $NbSe_2$. Electric polarizations were derived using the Berry phase method (64).

Experimental estimation of the polarization
By taking the two nearby DWs and the area between them as a parallel-plate capacitor filled with a homogeneous dielectric, the IP polarization could be calculated by the equation $P = (\varepsilon_r - 1)\varepsilon_0 V / d$, where ε_r is the relative permittivity of VCl_3, ε_0 is the electric constant, and V / d is the electric field, in which V and d are the maximum energy shift and the corresponding distance between the two opposite neighboring DWs (65). Because the ε_0 of VCl_3 is unknown, we took the value for $CrCl_3$ ($\varepsilon_0 = 8$) in our approximation calculations (66).

Supplementary Materials

This PDF file includes:
Supplementary Text
Figs. S1 to S20
References

REFERENCES AND NOTES

1. D. Zhang, P. Schoenherr, P. Sharma, J. Seidel, Ferroelectric order in van der Waals layered materials. *Nat. Rev. Mater.* **8**, 25–40 (2023).
2. P. Man, L. Huang, J. Zhao, T. H. Ly, Ferroic phases in two-dimensional materials. *Chem. Rev.* **123**, 10990–11046 (2023).
3. C. Gong, L. Li, Z. Li, H. Ji, A. Stern, Y. Xia, T. Cao, W. Bao, C. Wang, Y. Wang, Z. Q. Qiu, R. J. Cava, S. G. Louie, J. Xia, X. Zhang, Discovery of intrinsic ferromagnetism in two-dimensional van der Waals crystals. *Nature* **546**, 265–269 (2017).
4. B. Huang, G. Clark, E. Navarro-Moratalla, D. R. Klein, R. Cheng, K. L. Seyler, D. Zhong, E. Schmidgall, M. A. McGuire, D. H. Cobden, W. Yao, D. Xiao, P. Jarillo-Herrero, X. Xu, Layer-dependent ferromagnetism in a van der Waals crystal down to the monolayer limit. *Nature* **546**, 270–273 (2017).
5. K. Chang, J. Liu, H. Lin, N. Wang, K. Zhao, A. Zhang, F. Jin, Y. Zhong, X. Hu, W. Duan, Q. Zhang, L. Fu, Q.-K. Xue, X. Chen, S.-H. Ji, Discovery of robust in-plane ferroelectricity in atomic-thick SnTe. *Science* **353**, 274–278 (2016).
6. Z. Fei, W. Zhao, T. A. Palomaki, B. Sun, M. K. Miller, Z. Zhao, J. Yan, X. Xu, D. H. Cobden, Ferroelectric switching of a two-dimensional metal. *Nature* **560**, 336–339 (2018).
7. J. Qi, H. Wang, X. Chen, X. Qian, Two-dimensional multiferroic semiconductors with coexisting ferroelectricity and ferromagnetism. *Appl. Phys. Lett.* **113**, 043102 (2018).
8. M. Xu, C. Huang, Y. Li, S. Liu, X. Zhong, P. Jena, E. Kan, Y. Wang, Electrical control of magnetic phase transition in a type-I multiferroic double-metal trihalide monolayer. *Phys. Rev. Lett.* **124**, 067602 (2020).
9. J.-J. Zhang, L. Lin, Y. Zhang, M. Wu, B. I. Yakobson, S. Dong, Type-II multiferroic $Hf_2VC_2F_2$ MXene monolayer with high transition temperature. *J. Am. Chem. Soc.* **140**, 9768–9773 (2018).
10. Q. Song, C. A. Occhialini, E. Ergeçen, B. Ilyas, D. Amoroso, P. Barone, J. Kapeghian, K. Watanabe, T. Taniguchi, A. S. Botana, S. Picozzi, N. Gedik, R. Comin, Evidence for a single-layer van der Waals multiferroic. *Nature* **602**, 601–605 (2022).
11. M.-P. Miao, N. Liu, W.-H. Zhang, D.-B. Wang, W. Ji, Y.-S. Fu, Spin-resolved imaging of atomic-scale helimagnetism in monolayer NiI_2. arXiv:2309.16526 (2023).
12. M. Amini, A. O. Fumega, H. González-Herrero, V. Vaňo, S. Kezilebieke, J. L. Lado, P. Liljeroth, Atomic-scale visualization of multiferroicity in monolayer nil2. *Adv. Mater.* **36**, e2311342 (2024).
13. Y. Jiang, Y. Wu, J. Zhang, J. Wei, B. Peng, C.-W. Qiu, Dilemma in optical identification of single-layer multiferroics. *Nature* **619**, E40–E43 (2023).
14. S. Wu, X. Chen, C. Hong, X. Hou, Z. Wang, Z. Sheng, Z. Sun, Y. Guo, S. Wu, Layer thickness crossover of type-II multiferroic magnetism in C. arXiv:2307.10686 (2023).
15. H. Ju, Y. Lee, K.-T. Kim, I. H. Choi, C. J. Roh, S. Son, P. Park, J. H. Kim, T. S. Jung, J. H. Kim, K. H. Kim, J.-G. Park, J. S. Lee, Possible persistence of multiferroic order down to bilayer limit of van der Waals Material NiI_2. *Nano Lett.* **21**, 5126–5132 (2021).
16. N. Liu, C. Wang, C. Yan, C. Xu, J. Hu, Y. Zhang, W. Ji, Competing Multiferroic Phases in NiI_2 Mono- and Few-layers. arXiv:2211.14423 (2023).
17. L. Song, Y. Zhao, B. Xu, R. Du, H. Li, W. Feng, J. Yang, X. Li, Z. Liu, X. Wen, Y. Peng, Y. Wang, H. Sun, L. Huang, Y. Jiang, Y. Cai, X. Jiang, J. Shi, J. He, Robust multiferroic in interfacial modulation synthesized wafer-scale one-unit-cell of chromium sulfide. *Nat. Commun.* **15**, 721 (2024).
18. C. Huang, Y. Du, H. Wu, H. Xiang, K. Deng, E. Kan, Prediction of intrinsic ferromagnetic ferroelectricity in a transition-metal halide monolayer. *Phys. Rev. Lett.* **120**, 147601 (2018).
19. L. Camerano, G. Profeta, Symmetry breaking in vanadium trihalides. *2D Mater.* **11**, 025027 (2024).
20. C. Huang, F. Wu, S. Yu, P. Jena, E. Kan, Discovery of twin orbital-order phases in ferromagnetic semiconducting VI_3 monolayer. *Phys. Chem. Chem. Phys.* **22**, 512–517 (2020).
21. S. Son, M. J. Coak, N. Lee, J. Kim, T. Y. Kim, H. Hamidov, H. Cho, C. Liu, D. M. Jarvis, P. A. C. Brown, J. H. Kim, C.-H. Park, D. I. Khomskii, S. S. Saxena, J.-G. Park, Bulk properties of the van der Waals hard ferromagnet VI_3. *Phys. Rev. B* **99**, 041402(R) (2019).
22. T. Kong, K. Stolze, E. I. Timmons, J. Tao, D. Ni, S. Guo, Z. Yang, R. Prozorov, R. J. Cava, VI_3—A new layered ferromagnetic semiconductor. *Adv. Mater.* **31**, 1808074 (2019).
23. S. Tian, J.-F. Zhang, C. Li, T. Ying, S. Li, X. Zhang, K. Liu, H. Lei, Ferromagnetic van der Waals crystal VI_3. *J. Am. Chem. Soc.* **141**, 5326–5333 (2019).
24. M. Kratochvilova, P. Dolezal, D. Hovančík, J. Pospíšil, A. Bendová, M. Dušek, V. Holy, V. Sechovsky, Crystal structure evolution in the van der Waals vanadium trihalides. *J. Phys. Condens. Matter* **34**, 294007 (2022).
25. B. Lyu, L. Wang, Y. Gao, S. Guo, X. Zhou, Z. Hao, S. Wang, Y. Zhao, L. Huang, J. Shao, M. Huang, Structural and magnetic phase transitions in quasi-two-dimensional VBr_3. *Phys. Rev. B* **106**, 085430 (2022).
26. D. Mastrippolito, L. Camerano, H. Świątek, B. Šmíd, T. Klimczuk, L. Ottaviano, G. Profeta, Polaronic and Mott insulating phase of layered magnetic vanadium trihalide VCl_3. *Phys. Rev. B* **108**, 045126 (2023).
27. A. De Vita, T. T. P. Nguyen, R. Sant, G. M. Pierantozzi, D. Amoroso, C. Bigi, V. Polewczyk, G. Vinai, L. T. Nguyen, T. Kong, J. Fujii, I. Vobornik, N. B. Brookes, G. Rossi, R. J. Cava, F. Mazzola, K. Yamauchi, S. Picozzi, G. Panaccione, Influence of orbital character on the ground state electronic properties in the van der Waals transition metal iodides VI_3 and CrI_3. *Nano Lett.* **22**, 7034–7041 (2022).
28. Z. Lin, B. Huang, K. Hwangbo, Q. Jiang, Q. Zhang, Z. Liu, Z. Fei, H. Lv, A. Millis, M. McGuire, D. Xiao, J.-H. Chu, X. Xu, Magnetism and its structural coupling effects in 2D Ising ferromagnetic insulator VI_3. *Nano Lett.* **21**, 9180–9186 (2021).
29. J. Qiao, X. Kong, Z.-X. Hu, F. Yang, W. Ji, High-mobility transport anisotropy and linear dichroism in few-layer black phosphorus. *Nat. Commun.* **5**, 4475 (2014).
30. Z.-X. Hu, X. Kong, J. Qiao, B. Normand, W. Ji, Interlayer electronic hybridization leads to exceptional thickness-dependent vibrational properties in few-layer black phosphorus. *Nanoscale* **8**, 2740–2750 (2016).
31. J. He, S. Ma, P. Lyu, P. Nachtigall, Unusual Dirac half-metallicity with intrinsic ferromagnetism in vanadium trihalide monolayers. *J. Mater. Chem. C* **4**, 2518–2526 (2016).
32. W. Chen, Z. Sun, Z. Wang, L. Gu, X. Xu, S. Wu, C. Gao, Direct observation of van der Waals stacking–dependent interlayer magnetism. *Science* **366**, 983–987 (2019).
33. P. Li, C. Wang, J. Zhang, S. Chen, D. Guo, W. Ji, D. Zhong, Single-layer CrI_3 grown by molecular beam epitaxy. *Sci. Bull.* **65**, 1064–1071 (2020).
34. S. Lu, D. Guo, Z. Cheng, Y. Guo, C. Wang, J. Deng, Y. Bai, C. Tian, L. Zhou, Y. Shi, J. He, W. Ji, C. Zhang, Controllable dimensionality conversion between 1D and 2D $CrCl_3$ magnetic nanostructures. *Nat. Commun.* **14**, 2465 (2023).
35. F. E. Olsson, M. Persson, J. Repp, G. Meyer, Scanning tunneling microscopy and spectroscopy of NaCl overlayers on the stepped Cu(311) surface: Experimental and theoretical study. *Phys. Rev. B* **71**, 075419 (2005).
36. Z. Zhang, J. Nie, Z. Zhang, Y. Yuan, Y.-S. Fu, W. Zhang, Atomic visualization and switching of ferroelectric order in β-In_2Se_3 films at the single layer limit. *Adv. Mater.* **34**, e2106951 (2022).
37. D. Huo, Y. Bai, X. Lin, J. Deng, Z. Pan, C. Zhu, C. Liu, H. Yu, C. Zhang, Tuning of the valley structures in monolayer In_2Se_3/WSe_2 heterostructures via ferroelectricity. *Nano Lett.* **22**, 7261–7267 (2022).
38. J. Gou, H. Bai, X. Zhang, Y. L. Huang, S. Duan, A. Ariando, S. A. Yang, L. Chen, Y. Lu, A. T. S. Wee, Two-dimensional ferroelectricity in a single-element bismuth monolayer. *Nature* **617**, 67–72 (2023).
39. K. Chang, F. Küster, B. J. Miller, J.-R. Ji, J.-L. Zhang, P. Sessi, S. Barraza-Lopez, S. S. P. Parkin, Microscopic manipulation of ferroelectric domains in SnSe monolayers at room temperature. *Nano Lett.* **20**, 6590–6597 (2020).
40. Z. Zheng, Q. Ma, Z. Bi, S. de la Barrera, M.-H. Liu, N. Mao, Y. Zhang, N. Kiper, K. Watanabe, T. Taniguchi, J. Kong, W. A. Tisdale, R. Ashoori, N. Gedik, L. Fu, S.-Y. Xu, P. Jarillo-Herrero, Unconventional ferroelectricity in moiré heterostructures. *Nature* **588**, 71–76 (2020).
41. T. Kong, S. Guo, D. Ni, R. J. Cava, Crystal structure and magnetic properties of the layered van der Waals compound VBr_3. *Phys. Rev. Mater.* **3**, 084419 (2019).
42. A. R. Wildes, V. Simonet, E. Ressouche, R. Ballou, G. J. McIntyre, The magnetic properties and structure of the quasi-two-dimensional antiferromagnet $CoPS_3$. *J. Phys. Condens. Matter* **29**, 455801 (2017).
43. Y. Wang, Y. Huang, Y. Song, X. Zhang, Y. Ma, J. Liang, Y. Chen, Room-temperature ferromagnetism of graphene. *Nano Lett.* **9**, 220–224 (2009).
44. J. Červenka, M. I. Katsnelson, C. F. J. Flipse, Room-temperature ferromagnetism in graphite driven by two-dimensional networks of point defects. *Nat. Phys.* **5**, 840–844 (2009).
45. M. M. Ugeda, A. J. Bradley, S.-F. Shi, F. H. da Jornada, Y. Zhang, D. Y. Qiu, W. Ruan, S.-K. Mo, Z. Hussain, Z.-X. Shen, F. Wang, S. G. Louie, M. F. Crommie, Giant bandgap renormalization and excitonic effects in a monolayer transition metal dichalcogenide semiconductor. *Nat. Mater.* **13**, 1091–1095 (2014).
46. Y. Zhao, J. Qiao, P. Yu, Z. Hu, Z. Lin, S. P. Lau, Z. Liu, W. Ji, Y. Chai, Extraordinarily strong interlayer interaction in 2D layered PtS_2. *Adv. Mater.* **28**, 2399–2407 (2016).
47. B. Li, Z. Wan, C. Wang, P. Chen, B. Huang, X. Cheng, Q. Qian, J. Li, Z. Zhang, G. Sun, B. Zhao, H. Ma, R. Wu, Z. Wei, Y. Liu, L. Liao, Y. Ye, Y. Huang, X. Xu, X. Duan, W. Ji, X. Duan, Van der Waals epitaxial growth of air-stable $CrSe_2$ nanosheets with thickness-tunable magnetic order. *Nat. Mater.* **20**, 818–825 (2021).
48. L. Rogée, L. Wang, Y. Zhang, S. Cai, P. Wang, M. Chhowalla, W. Ji, S. P. Lau, Ferroelectricity in untwisted heterobilayers of transition metal dichalcogenides. *Science* **376**, 973–978 (2022).
49. Y. Li, Q. Yuan, D. Guo, C. Lou, X. Cui, G. Mei, H. Petek, L. Cao, W. Ji, M. Feng, 1D electronic flat bands in untwisted Moiré superlattices. *Adv. Mater.* **35**, e2300572 (2023).
50. D. Guo, C. Wang, L. Wang, Y. Lu, H. Wu, Y. Zhang, W. Ji, Orbital-ordering driven simultaneous tunability of magnetism and electric polarization in strained monolayer VCl_3. *Chin. Phys. Lett.* **41**, 047501 (2024).
51. M. Wu, J. Li, Sliding ferroelectricity in 2D van der Waals materials: Related physics and future opportunities. *Proc. Natl. Acad. Sci. U.S.A.* **118**, e2115703118 (2021).

52. T. Zhao, A. Scholl, F. Zavaliche, K. Lee, M. Barry, A. Doran, M. P. Cruz, Y. H. Chu, C. Ederer, N. A. Spaldin, R. R. Das, D. M. Kim, S. H. Baek, C. B. Eom, R. Ramesh, Electrical control of antiferromagnetic domains in multiferroic BiFeO₃ films at room temperature. *Nat. Mater.* **5**, 823–829 (2006).

53. Y. Huang, Y.-H. Pan, R. Yang, L.-H. Bao, L. Meng, H.-L. Luo, Y.-Q. Cai, G.-D. Liu, W.-J. Zhao, Z. Zhou, L.-M. Wu, Z.-L. Zhu, M. Huang, L.-W. Liu, L. Liu, P. Cheng, K.-H. Wu, S.-B. Tian, C.-Z. Gu, Y.-G. Shi, Y.-F. Guo, Z. G. Cheng, J.-P. Hu, L. Zhao, G.-H. Yang, E. Sutter, P. Sutter, Y.-L. Wang, W. Ji, X.-J. Zhou, H.-J. Gao, Universal mechanical exfoliation of large-area 2D crystals. *Nat. Commun.* **11**, 2453 (2020).

54. Q. Fu, J.-Q. Dai, X.-Y. Huang, Y.-Y. Dai, Y.-H. Pan, L.-L. Yang, Z.-Y. Sun, T.-M. Miao, M.-F. Zhou, L. Zhao, W.-J. Zhao, X. Han, J.-P. Lu, H.-J. Gao, X.-J. Zhou, Y.-L. Wang, Z.-H. Ni, W. Ji, Y. Huang, One-step exfoliation method for plasmonic activation of large-area 2D crystals. *Adv. Sci.* **9**, 2204247 (2022).

55. Q. Wang, W. Zhang, L. Wang, K. He, X. Ma, Q. Xue, Large-scale uniform bilayer graphene prepared by vacuum graphitization of 6H-SiC(0001) substrates. *J. Phys. Condens. Matter* **25**, 095002 (2013).

56. W. Wan, P. Dreher, D. Muñoz-Segovia, R. Harsh, H. Guo, A. J. Martínez-Galera, F. Guinea, F. de Juan, M. M. Ugeda, Observation of superconducting collective modes from competing pairing instabilities in single-layer NbSe₂. *Adv. Mater.* **34**, e2206078 (2022).

57. D. Nečas, P. Klapetek, Gwyddion: An open-source software for SPM data analysis. *Open Phys.* **10**, 181–188 (2012).

58. J. P. Perdew, K. Burke, M. Ernzerhof, Generalized gradient approximation made simple. *Phys. Rev. Lett.* **77**, 3865–3868 (1996).

59. P. E. Blöchl, Projector augmented-wave method. *Phys. Rev. B* **50**, 17953–17979 (1994).

60. G. Kresse, J. Furthmüller, Efficient iterative schemes for *ab initio* total-energy calculations using a plane-wave basis set. *Phys. Rev. B* **54**, 11169–11186 (1996).

61. S. Grimme, J. Antony, S. Ehrlich, H. Krieg, A consistent and accurate *ab initio* parametrization of density functional dispersion correction (DFT-D) for the 94 elements H-Pu. *J. Chem. Phys.* **132**, 154104 (2010).

62. V. I. Anisimov, F. Aryasetiawan, A. I. Lichtenstein, First-principles calculations of the electronic structure and spectra of strongly correlated systems: The LDA+ *U* method. *J. Phys. Condens. Matter* **9**, 767–808 (1997).

63. Y. Yekta, H. Hadipour, E. Şaşıoğlu, C. Friedrich, S. A. Jafari, S. Blügel, I. Mertig, Strength of effective Coulomb interaction in two-dimensional transition-metal halides MX_2 and MX_3 (M = Ti, V, Cr, Mn, Fe, Co, Ni; X = Cl, Br, I). *Phys. Rev. Mater.* **5**, 034001 (2021).

64. R. D. King-Smith, D. Vanderbilt, Theory of polarization of crystalline solids. *Phys. Rev. B* **47**, 1651–1654 (1993).

65. R. P. Feynman, R. B. Leighton, M. Sands, *The Feynman Lectures on Physics, Vol. II: The New Millennium Edition: Mainly Electromagnetism and Matter*, The Feynman Lectures on Physics (Basic Books, 2011); https://books.google.com/books?id=hlRhwGK40fgC.

66. A. Borghesi, G. Guizzetti, F. Marabelli, L. Nosenzo, E. Reguzzoni, Far-infrared optical properties of CrCl₃ and CrBr₃. *Solid State Commun.* **52**, 463–465 (1984).

67. A. Yajima, R. Matsuzaki, Y. Saeki, The thermal decomposition of vanadium(III) chloride oxide and its reaction with oxygen. *Bull. Chem. Soc. Jpn.* **52**, 3292–3295 (1979).

68. S. Jiang, G. Wang, H. Deng, K. Liu, Q. Yang, E. Zhao, L. Zhu, W. Guo, J. Yang, C. Zhang, H. Wang, X. Zhang, J.-F. Dai, G. Luo, Y. Zhao, J. Lin, General synthesis of 2D magnetic transition metal dihalides via trihalide reduction. *ACS Nano* **17**, 363–371 (2023).

69. C. Zhang, A. Johnson, C.-L. Hsu, L.-J. Li, C.-K. Shih, Direct imaging of band profile in single layer MoS₂ on graphite: Quasiparticle energy gap, metallic edge states, and edge band bending. *Nano Lett.* **14**, 2443–2447 (2014).

70. M.-H. Chiu, C. Zhang, H.-W. Shiu, C.-P. Chuu, C.-H. Chen, C.-Y. S. Chang, C.-H. Chen, M.-Y. Chou, C.-K. Shih, L.-J. Li, Determination of band alignment in the single-layer MoS₂/WSe₂ heterojunction. *Nat. Commun.* **6**, 7666 (2015).

71. R. M. Feenstra, Tunneling spectroscopy of the (110) surface of direct-gap III-V semiconductors. *Phys. Rev. B* **50**, 4561–4570 (1994).

72. A. Soumyanarayanan, M. M. Yee, Y. He, J. van Wezel, D. J. Rahn, K. Rossnagel, E. W. Hudson, M. R. Norman, J. E. Hoffman, Quantum phase transition from triangular to stripe charge order in NbSe₂. *Proc. Natl. Acad. Sci.* **110**, 1623–1627 (2013).

73. T. Sluka, P. Bednyakov, P. Yudin, A. Crassous, A. Tagantsev, "Charged Domain Walls in Ferroelectrics" in *Topological Structures in Ferroic Materials: Domain Walls, Vortices and Skyrmions*, J. Seidel, Ed. (Springer International Publishing, 2016), pp. 103–138; https://doi.org/10.1007/978-3-319-25301-5_5.

74. S. Zhong, X. Zhang, J. Gou, L. Chen, S.-H. Wei, S. A. Yang, Y. Lu, Lone-pair activated ferroelectricity and stable charged domain wall in Bi monolayer. *Nat. Commun.* **15**, 8322 (2024).

75. R. Cheng, L. Yin, Y. Wen, B. Zhai, Y. Guo, Z. Zhang, W. Liao, W. Xiong, H. Wang, S. Yuan, J. Jiang, C. Liu, J. He, Ultrathin ferrite nanosheets for room-temperature two-dimensional magnetic semiconductors. *Nat. Commun.* **13**, 5241 (2022).

76. Z. Li, L. Chen, S. Meng, L. Guo, J. Huang, Y. Liu, W. Wang, X. Chen, Field and temperature dependence of intrinsic diamagnetism in graphene: Theory and experiment. *Phys. Rev. B* **91**, 094429 (2015).

77. X. Zhang, Q. Lu, W. Liu, W. Niu, J. Sun, J. Cook, M. Vaninger, P. F. Miceli, D. J. Singh, S.-W. Lian, T.-R. Chang, X. He, J. Du, L. He, R. Zhang, G. Bian, Y. Xu, Room-temperature intrinsic ferromagnetism in epitaxial CrTe₂ ultrathin films. *Nat. Commun.* **12**, 2492 (2021).

78. R. Basnet, A. Wegner, K. Pandey, S. Storment, J. Hu, Highly sensitive spin-flop transition in antiferromagnetic van der Waals material MPS_3 (M = Ni and Mn). *Phys. Rev. Mater.* **5**, 064413 (2021).

79. V. W. Brar, Y. Zhang, Y. Yayon, T. Ohta, J. L. McChesney, A. Bostwick, E. Rotenberg, K. Horn, M. F. Crommie, Scanning tunneling spectroscopy of inhomogeneous electronic structure in monolayer and bilayer graphene on SiC. *Appl. Phys. Lett.* **91**, 122102 (2007).